Structural Diversity in a New Series of Halogenated Quinolyl Salicylaldimides-Based FeIII Complexes Showing Solid-State Halogen- Bonding/Halogen···Halogen Interactions

Suchithra Ashoka Sahadevan, Enzo Cadoni, Noemi Monni, Cristina Saenz de Pipaon, Jose-Ramon Galan Mascaros, Alexandre Abherve, Narcis Avarvari, Luciano Marchio, Massimiliano Arca, and Maria Laura Mercuri

Dipartimento di Scienze Chimiche e Geologiche, Universita` degli Studi di Cagliari, S.S. 554 Bivio per Sestu, I09042 Monserrato, Cagliari, Italy

Laboratoire MOLTECH-Anjou UMR 6200, UFR Sciences, CNRS, Universite´ d'Angers, Bat. K, 2 Bd. Lavoisier, 49045 Angers, France

Institute of Chemical Research of Catalonia, Barcelona Institute of Science and Technology, Avinguda Paısos Catalans 16, Tarragona 43007, Spain

Institucio´ Catalana de Recerca i Estudis Avancats, Passeig Lluis Companys 23, Barcelona 08010, Spain

Dipartimento SCVSA, Universita` di Parma, Parco Area delle Scienze 17A, I43124 Parma, Italy

✶ Supporting Information

ABSTRACT: A new series of tridentate N-8-quinolyl-salicylaldimine ligands, Hqsal-5,7-X_2 [X = Cl(1), Br(2), I(3)], halo-substituted at the 5,7 position of the aminoquinoline moiety and their corresponding complexes with Fe^{III} were synthesized and formulated as $[Fe(qsal-5,7-X_2)(NCS)(MeO)]_2 \cdot$solv. (X = Cl (1a), Br (2a), I (3a, solv = $^1/_2$MeOH), $[Fe_4(qsal-5,7-X_2)_4(NCS)_2(MeO)_2] \cdot$solv. (X = Br (2b), I (3b; solv = $4CH_2Cl_2$)) by single-crystal X-ray diffraction analysis. 1a and 2a are isostructural dimers where each Fe^{III} metal ion, showing a distorted octahedral environment, is bound by a N,N,O tridentate $(qsal-5,7-X_2)^-$ (X = Cl and Br) ligand, a N-coordinated SCN^- anion, and a bridging methanolate anion. 2b and 3b are centrosymmetric tetramers where each Fe^{III} is bound by three nitrogen atoms and three

oxygen atoms derived from a tridentate $(qsal-5,7-X_2)^-$ (X = Br and I), a SCN^-, a bridging methanolate anion, and a bridging μ^2-oxy moiety. In 3b, the iodine atoms dominate the packing interactions through the establishment of a halogen-bonding network. The magnetic behavior of 1a−3a dimers and 2b−3b tetramers indicate the presence of strong antiferromagnetic interactions between Fe^{III} centers (S = 5/2), mediated by the alkoxy bridges. Experimental data can be modeled with an isotropic Hamiltonian, $H = -2J(S_1 \cdot S_2)$ for dimers (J = −15 cm^{-1}) and $H = -2J(S_2 \cdot S_3) - 2J'(S_1 \cdot S_2 + S_3 \cdot S_4)$, for tetramers (J = −24 cm^{-1}, J′ = −11 cm^{-1}). The magnetic behavior of 1a−3a dimers indicates the presence of strong antiferromagnetic interactions between Fe^{III} centers (S = 5/2), mediated by the alkoxy bridges. 2b and 3b show the same magnetic behavior since they contains analogous bridges between paramagnetic centers, but for a linear tetramer. Density functional theory (DFT) calculations, based on hybrid functional mPW1PW paralleled by the Def2SVP all-electron split-valence basis sets, support the experimental results, showing that monomers could possibly show a spin crossover (SCO) behavior, even though the formation of complexes with an even number of metal ions results in the strong antiferromagnetic interactions. Accordingly, broken symmetry DFT calculations carried out on 1a clearly show that the antiferromagnetic coupling of the two HS Fe^{III} centers results in the lowest energy electron configuration of the complex.

INTRODUCTION

One of the most powerful strategies to design halogen-bonded systems is based on the use of tectons, in particular, metallotectons, namely, metal complexes bearing peripheral halogen atoms, able to be involved in well identified noncovalent intermolecular interactions, such as halogen bonds. Over the past decade, halogen bonding (XB), a strong, specific, and highly directional noncovalent interaction, has gained great interest among the known noncovalent bonds, for the construction of one-, two-, and three-dimensional (1D, 2D, and 3D) self-assembled supramolecular architectures.[1−4] This interaction

plays a role as crucial as hydrogen bonding (HB)[5] in driving highly specific crystal packing patterns and several applications of XB have been reported[1] in various research areas such as materials science and synthetic chemistry. Halogen···halogen (XX) interactions are also a peculiar class of halogens bonds interactions, which, although weak, play a key role in the formation of supramolecular networks ranging from one- to three-dimensional (1D to 3D) materials to self-assembled monolayers and can be considered as a reliable supramolecular tool in molecular self-assembly.[6−9] In this context the combination of halo-substituted anilates, the 3,6-dihalo derivatives of 2,5-dihydroxybenzoquinone ($H_4C_6O_4$), X_2An^{2-} (X = Cl, Br, I), with paramagnetic metals has been shown to be particularly successful.[10−15] In the search of novel halo-substituted tectons where the halogen atoms can play a role on the crystalline packing pattern and/or physical properties, we focused our attention on the tridentate N-8-quinolyl-5-X-salicylaldiminate (X = H, Hqsal) ligand and its halo-substituted derivatives on the 5-salicylaldiminate moiety (qsal-X) (X = F, Cl, Br, I), because of the interesting spin crossover (SCO) properties shown by their Fe^{III}/Fe^{II} complexes.[16−21] Temperature-induced spin transition in fact was observed in [Fe(qsal)$_2$]NCS and [Fe(qsal)$_2$]NCSe[22−25] with a wide thermal hysteresis loop of 140 and 180 K respectively, while switching the spin state upon exposure to light (LIESST effect) was also found.[24] Halogen effects on the SCO behavior were reported in [Fe^{III}(qsal-X)$_2$]NCS·solvent (X = F, Cl, Br; solvent = $^1/_4$CH$_2$Cl$_2$·$^1/_2$MeOH) complexes, as the spin transition temperature was found to increase on going from F to Br.[17,26−31] Very recently, an abrupt two-step SCO above room temperature[32,33] was observed in the [Fe^{II}(qsal-Cl)$_2$] complex due to the halogen substitution on the salicylaldiminate moiety of the ligand that has the potential to improve the SCO properties within Fe^{II}−SCO systems. Therefore, the introduction of halogen atoms at certain key positions of the metal complexes influences their physical properties significantly, although keeping their structure unaltered. In this work we investigate the influence of the halogen substitution on the quinolyl moiety of the Hqsal ligand, which has never been studied so far, with the aim to highlight how a simple change in the positions of the halogen atoms in the same ligand can dramatically change the crystal structure and physical properties of the related metal complexes. We report herein the synthesis and structural characterization of the novel class of halo-substituted Hqsal-5,7-X$_2$ ligands (X = Cl, 1, Br, 2, I, 3), shown in Chart 1, and their Fe^{III} complexes: [Fe(qsal-Cl$_2$)(NCS)(MeO)]$_2$ (1a), [Fe(qsal-5,7-Br$_2$)(NCS)(MeO)]$_2$ (2a), [Fe$_4$(qsal-5,7-Br)$_4$(NCS)$_2$(MeO)$_2$] (2b), [Fe(qsal-5,7-I$_2$)(NCS)(MeO)]$_2$, (3a,·$^1/_2$MeOH), and [Fe$_4$(qsal-5,7-I$_2$)$_4$-
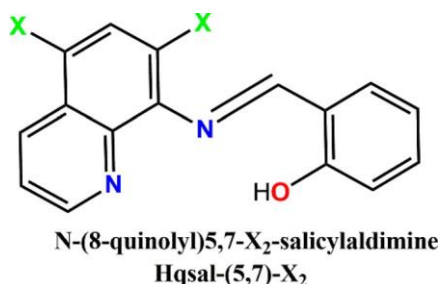
(NCS)$_2$(MeO)$_2$] (3b,·4CH$_2$Cl$_2$). The magnetic properties of the 1a−3a and 2b−3b complexes are also reported.

RESULTS AND DISCUSSION

Synthesis of Hqsal-5,7-X$_2$ Ligands and Their Fe^{III} Complexes. An overview of the synthetic procedure of the Hqsal-5,7-X$_2$ ligands is shown in Scheme 1.

The halo-substituted Hqsal-5,7-X$_2$ ligands were prepared in good yields (48−89%) by treating 5,7-dihalo-8-aminoquinoline in EtOH with salicylaldehyde and glacial acetic acid. The synthesis of the Hqsal-5,7-X$_2$ ligands was performed according to the synthetic pathway shown in Scheme S1 in Supporting Information. The first stage of the process is a simple formation of an imine, starting from amine and aldehyde, at room temperature and with good yields despite the substituents used. The reaction is carried out in ethanol and in the presence of acetic acid. Acetic acid was used both for increasing the electrophilicity of the carbonyl aldehyde group, given the low nucleophilicity of the aromatic amine, and for favoring the water elimination in the second stage. The reagents and the products are poorly soluble in ethyl alcohol, and therefore reaction times of almost 24 h are required for the complete disappearance of the amines as reported in Scheme S2 in Supporting Information. More details on the synthesis[34−37] are given in Supporting Information.

The Fe^{III} complexes, 1a−3a and 2b−3b, were synthesized according to the general synthetic strategy recently reported for analogous complexes[20] (Scheme 2).

These complexes were obtained by carefully layering the ligands 1−3 with Et$_3$N in CH$_2$Cl$_2$ and on top FeCl$_3$·6H$_2$O and NaSCN in a 1:1 ratio, dissolved in MeOH. Electrospray ionization mass spectrometry (ESI-MS) spectra recorded on freshly prepared CHCl$_3$/MeOH solutions, in the 100−2000 m/z mass range, showed only the molecular ions, which can be assigned to [Fe(qsal-5,7-X$_2$)$_2$]$^+$ monomeric species [X = Cl (1c$^+$), Br (2c$^+$), and I (3c$^+$)]. Mass spectra recorded on solutions with concentration values at the upper solubility limit (10 mg/mL) and lower values of needle voltage of 4500 V did not show dimeric forms (vide infra). Therefore, to improve peak resolution, spectra were recorded in the 100−1000 m/z mass range. The isotopic patterns of the ligands 1−3 and of the monomeric species 1c$^+$, 2c$^+$, and 3c$^+$ are reported in Supporting Information (Figures S1−S2).

Structural Studies. Among the ligands, only single crystals of 3 could be obtained by recrystallization of the crude product in dichloromethane, confirming the expected composition (Figure S3).

Single crystals of the iron complexes were obtained by slow diffusion of ligand in dichloromethane and Fe^{III} salt with NaSCN in methanol. The X-ray diffraction analysis unexpectedly established the complexes to be dimers or tetramers according to Scheme 2 and Table 1.

The presence of halogen atoms on the ligands periphery expands the types of interactions that can be exchanged by the iron complexes.[38,39] Here, we will analyze the influence of the halogen substitution (Cl, Br, I) on the second coordination sphere and crystal packing.

The complexes 1a and 2a crystallize in the triclinic space group P$\bar{1}$; 2b crystallizes in monoclinic space group P2$_1$/c. The molecular structure of 1a is reported in Figure S4. The molecular structures of 2a, 3a, 2b, and 3b are reported in Figures 1, 2, and 3. A summary of X-ray crystallographic data for 3, 1a−3a, and 2b−3b are reported in Table S1, and selected bond distances (Å) and

Chart 1. Structure of Hqsal-5,7-X$_2$ Ligand[a]

N-(8-quinolyl)5,7-X$_2$-salicylaldimine
Hqsal-(5,7)-X$_2$

[a]X = Cl (1), Br (2), I (3).

Scheme 1. Overview of the Synthetic Procedure of Hqsal-5,7-X$_2$ Ligands
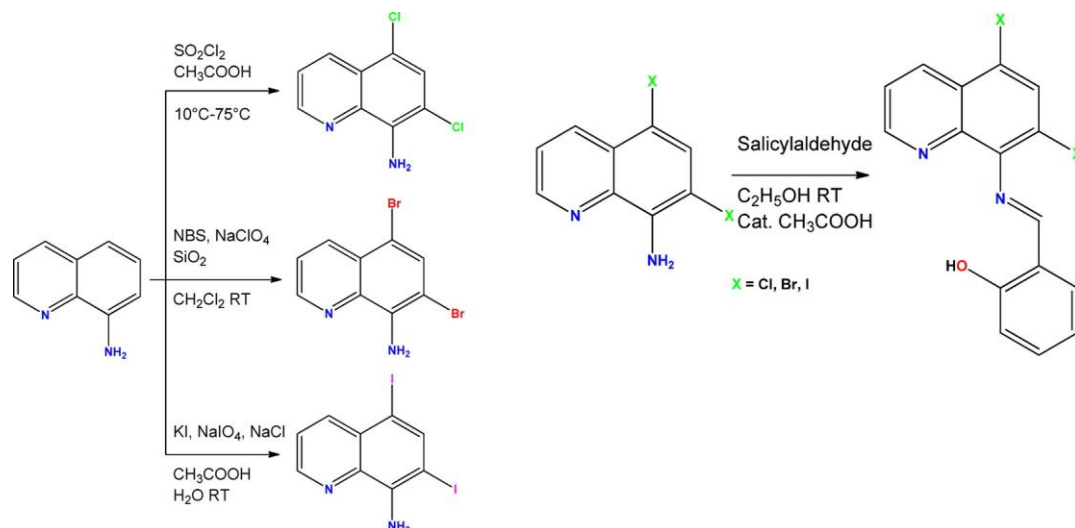
Scheme 2. General Synthetic Scheme for 1a−3a, 2b−3b Complexes[a]
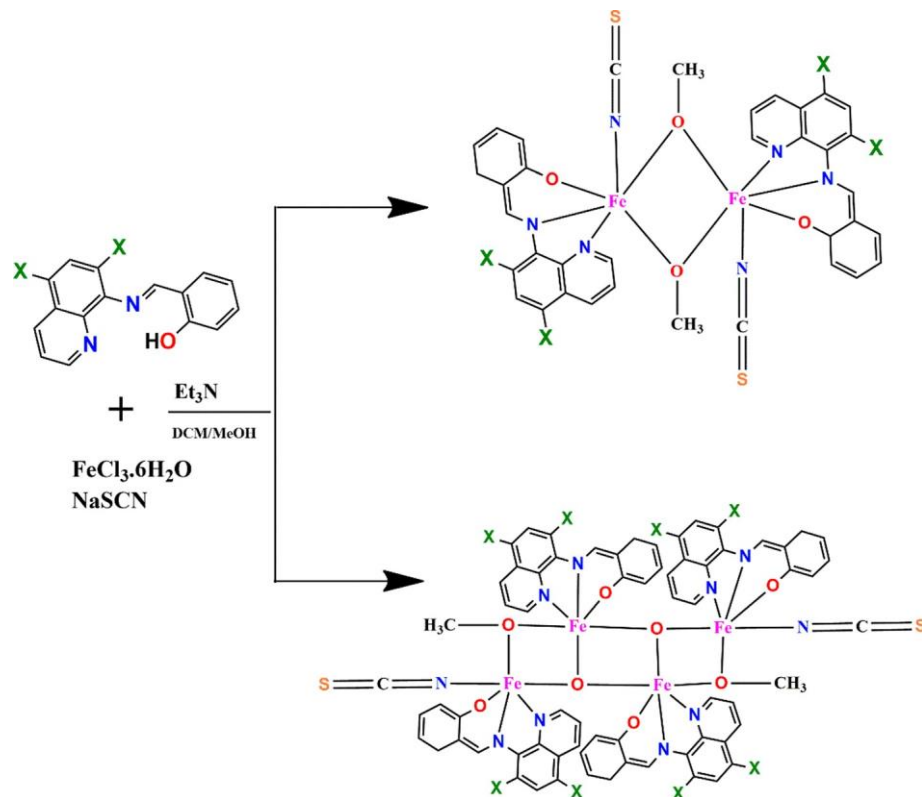
[a]X = Cl (1), Br (2), I (3); a = dimer; b = tetramer.

Table 1. Summary of the Obtained Fe^{III} Complexes

	FeCl$_3$·6H$_2$O + NaSCN		
	X = Cl	Br	I
[Fe(qsal-5,7-X$_2$)(NCS)(MeO)]$_2$ dimer	1a	2a	3a[a]
[Fe$_4$(qsal-5,7-X$_2$)$_4$(NCS)$_2$(MeO)$_2$] tetramer		2b	3b[b]

[a]Structurally characterized in 3a·$^1/_2$MeOH. [b]Structurally characterized in 3b·4CH$_2$Cl$_2$.

angles (deg) for 1a−3a and 2b−3b are reported in Tables S2−S7.

Compounds 1a and 2a are isostructural, and their molecular features can therefore be described together. Both complexes lie on an inversion center and half dimer represents the asymmetric unit. The Fe^{III} metal is in a distorted octahedral environment, and it is bound by a N,N,O tridentate ligand, a SCN$^-$ anion, and a bridging methanolate anion. For the tridentate ligand, the Fe−N bond distances are significantly longer (0.13−0.25 Å) than the remaining bond distances, and the shortest distance is that between the metal and the phenolate moiety, Table S2 in Supporting Information. The SCN$^-$ anion is bound to the metal center through the nitrogen atom, and consistently, it exhibits a

2a

3a
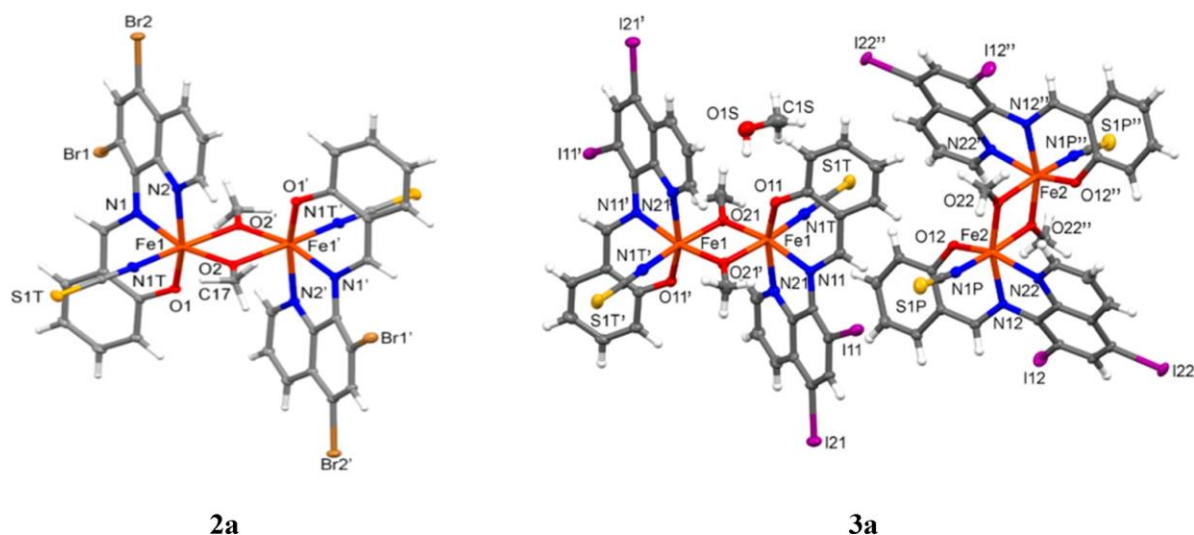
Figure 1. Molecular structure of 2a (symmetry code ′ = −x; 1 − y; 1 − z) and 3a (symmetry code ′ = 2 − x; 1 − y; −z, ″ = 1 − x; −y; 1 − z). Thermal ellipsoids are drawn at the 30% probability level. Color code: C = gray, Cl = green, Br = brown, O = red, S = yellow, Fe = orange, N = blue, H = white.

linear coordination geometry. The asymmetric unit of compound 3a comprises two half dimeric units and one methanol molecule of crystallization (Figure 1). The overall structural arrangement is nevertheless similar to that of 1a and 2a, since the presence of the iodine on the periphery of the aromatic rings has a negligible influence on the iron coordination environment. The methyl alcohol molecule forms a hydrogen bond with the oxygen atom of the phenolate moiety, O(11). In 1a−3a, the metal−metal distance is approximately 3.15 Å. The crystal packing of 1a and 2a is reported in Figure S5 and Figure 2. Adjacent molecules exchange different types of interactions, namely, Cl···Cl (3.39 Å) and Br···Br (3.51 Å) with symmetry related halogen atoms, CH···S with the aromatic ring and the SCN⁻ anion and π−π stacks with adjacent bromoquinoline rings. The crystal packing of 3a is more complex due to the presence of two different molecular entities and the solvent of crystallization. In this system, the presence of the iodine atom with respect to the bromine and chlorine in 1a and 2a expands the possible types of interactions that can be formed between adjacent molecules. In fact, I(22) and I(21) both interacts with S(1T) of the thiocyanate group. The geometry of the I(22)···S(1T) interaction (3.49 Å) is consistent with the presence of a halogen bond, whereas the geometry of the I(21)···S(1T) interaction (3.56 Å) presumably occurs through the negatively charged corona on iodine toward the terminal sulfur consistent with the presence of a chalcogenide bond.[1,4,40]

2b and 3b are centrosymmetric tetramers where the two outermost metal have a different coordination environment than the two innermost metals (Figure 3).

In 3b, four dichloromethane molecules of crystallization per tetrameric complex are present. In both systems Fe(1) is bound by three nitrogen atoms and three oxygen atoms derived from a N,N,O tridentate ligand, a SCN⁻ anion, a bridging methanolate, and a bridging oxy moiety. Differently, Fe(2) is bound by two nitrogen atoms and four oxygen atoms derived from a N,N,O tridentate ligand, two bridging oxy moieties, and a bridging methanolate anion. In both compounds, the Fe(1)−Fe(2) and Fe(2)−Fe(2)′ bond distances are 3.07 and 2.96 Å, respectively. The crystal packing of 2b is reported in Figure 4. Ideally, the molecules form layers by means of π−π stacks, CH···S, and CH··· C/N interactions between the aromatic ring and the SCN⁻

anion. These layers interact by forming halogen bond (Br(3)··· Br(4), 3.62 Å) and CH···Br (3.77 Å) interactions between symmetry related molecules.

In 3b, the iodine atoms dominate the packing interactions, as shown in Figure 5. According to the geometries of the interactions, the negative corona of I(1) interacts with the σ-hole of I(4) of a symmetry related molecule. Likewise, the lone pair distribution of S(1) interacts with the σ-hole of I(3).[1,4,40] Hence, I(3) acts as an XB donor with respect to the carbon atom of an adjacent SCN⁻ anion. Hence I(2), I(3), and I(4) act as XB donors, whereas I(1) acts as an XB acceptor. Dichloromethane molecules of crystallization are also involved in weak interactions among adjacent complex molecules.

Different views of the crystal packing of 3b are reported in Figure S6. In all ligand systems, the aromatic moieties linked by the imino group are not coplanar since they form a dihedral angle in the 31−41° range. In 2b and 3b, the tridentate ligands positioned on the same side with respect to the Fe$_4$O$_4$ core form π−π stacks with the quinoline and phenolate residues. The shortest contact is between the aromatic rings of the phenolate groups (3.4−3.5 Å range), whereas the distances between the quinoline groups is approximately 3.6 Å for 2b and greater than 3.7 Å for 3b.

Magnetic Measurements. In these series, compounds type a (dimers) and b (tetramers) are magnetically identical, if we consider the intermolecular magnetic interactions as negligible. Indeed, their magnetic behavior is indistinguishable within experimental error. Therefore, we only describe the magnetic properties of 1a and 2b, as representatives of these two magnetic structures.

The χT product for 1a at room temperature is 5.01 emu K mol⁻¹, lower than the expected value for the spin-only contribution of two high spin (HS) Fe^{III} S = 5/2 centers (χT_{HS} ≈ 8.750 emu K mol⁻¹), but significantly higher than the spin-only contribution of two low spin (LS) Fe^{III} S = 1/2 centers ($\chi T_{LS.}$ ≈ 0.750 emu K mol⁻¹). This confirms the HS state of the Fe^{III} centers and suggests the presence of strong antiferromagnetic interactions between them, mediated by the alkoxy bridges. In the 2−300 K range, χT decreases with temperature (Figure 6, left), reaching values close to zero at very low temperatures. The experimental data can be fitted to the Hamiltonian:
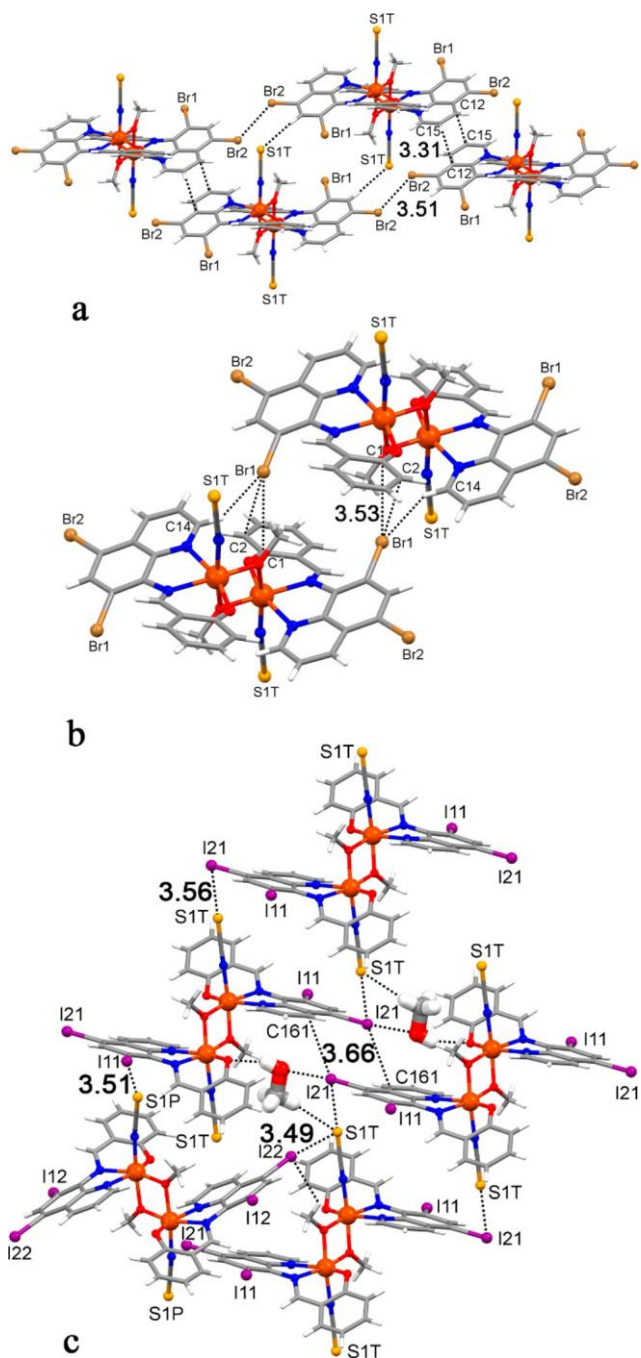
a

b

c

Figure 2. Portion of the crystal packing of 2a (a and b) and 3a (c), with the methanol molecule of crystallization highlighted. Dashed lines represent short interactions between symmetry related molecules. Selected weak interaction distances are indicated in Å.

$$H = -2J(S_1 \cdot S_2)$$

where $S_1 = S_2 = 5/2$. The best fit (Figure 6, left) was found for $g = 2.09$, $J = -21$ K (-14.6 cm^{-1}), with the addition of a small paramagnetic impurity, equivalent to ~2% of the total spin carriers.

The magnetic behavior for 2b is similar, since it contains analogous bridges between paramagnetic centers, but now in a linear tetramer. The room temperature χT product is 8.50 emu K mol^{-1}. This value can only be assigned to four HS Fe^{III} centers, antiferromagnetically coupled (χT$_{HS}$ ≈ 17.50 emu K mol^{-1}, χT$_{LS}$

≈ 1.50 emu K mol^{-1}). In this case, the appropriate phenomenological Hamiltonian is

$$H = -2J(S_2 \cdot S_3) - 2J'(S_1 \cdot S_2 + S_3 \cdot S_4)$$

where $S_1 = S_2 = S_3 = S_4 = 5/2$. The temperature dependence of the χT product was satisfactorily reproduced with parameters: $g = 2.03$, $J = -35$ K (24.3 cm^{-1}), $J' = -16$ K (11.1 cm^{-1}), and a paramagnetic impurity equivalent to ~2.5% of the total spin carriers (Figure 6, right). It is particularly significant the fact that the shape of the curve can be reproduced only if $J > J'$. We found a ratio of 2 between both exchange parameters as optimum to reproduce the data. This can be rationalized if we look into the Fe−O−Fe angles. Whereas the Fe1−O−Fe2 bridging angles are asymmetric (≈ 98° and 105°), the two Fe2−O−Fe2 angles are almost identical, forming a perfect square. This permits a better overlap between the magnetic orbitals, and a stronger antiferromagnetic superexchange in the central bridge.

DFT Calculations. In order to investigate the electronic structure and reactivity of the ligands 1−3 and the relevant iron(III) complexes, quantum-mechanical (QM) calculations were carried out at the density functional theory (DFT) level.[41] Previous theoretical investigations showed that the correct modeling of high/low spin equilibria at the DFT level depends dramatically on the choice of the functional,[42] which can unevenly favor one of the two spin states. In particular, it was observed that the pure functionals PW91[43,44] and BLYP[45] favor the LS state, while the paradigmatic hybrid functional B3LYP,[46−48] featuring a 20% Hartree−Fock (HF) exchange, favors the HS state.[37] Kepp comparatively examined 12 different functionals and demonstrated that the B3LYP* hybrid functional (HF exchange 15%)[49,50] provides an accurate evaluation of the HS-LS energy gap for 30 different SCO iron complexes.[51] This notwithstanding, in the peculiar case of qsal-X$^-$ (qsal-X$^-$ = monosubstituted quinolylsalicylaldiminate; X = H, OMe, F, Cl, Br, I) Fe^{III} tris-complexes, the B3LYP* functional was recently proven to overestimate the HS−LS enthalpy difference ΔH$_{SCO}$.[52] In this work, based on the very good results achieved in the past on a variety of both organic[53−55] and inorganic systems,[56−58] we turned to test the hybrid functional mPW1PW by Adamo and Barone,[59] paralleled by the Def2SVP all-electron split-valence BS, including polarization functions.[60]

Whatever the combination of BSs and functional, HS and LS configurations show different structural features, in particular, as far as the metal ion is involved, so that a comparison between theoretically optimized and structural metric parameters allows for the attribution of the correct spin state. A validation of the computational setup chosen for this work was therefore carried out by comparing the structural bond distances and angles determined for the complex [Fe(qsal-F)$_2$]$^+$ (4$^+$), isolated in 4(NCS),[17] featuring an LS at 100 K and a HS Fe^{III} center at 270 K, with the corresponding optimized metric parameters. An examination of the bond distances involving the central metal ion shows that on passing from LS to HS the Fe−N distances are sensibly modified [average values 1.960(2) and 1.983(2) Å at 100 and 270 K,[14] respectively], while the Fe−O bond lengths remain almost unaltered [average values 1.875(2) and 1.866(2) Å at 100 and 270 K,[14] respectively]. DFT optimized distances are in very good agreement with the structural ones and display the trend found experimentally on passing from LS to HS configurations [LS: Fe−N, 1.973; Fe−O 1.857; HS: Fe−N, 2.173; Fe−O, 1.898 Å]. Notably, the uncorrected total electronic energies of the LS and HS configurations calculated for 4$^+$ in the gas phase differ by only 2.80 kcal mol^{-1}, while the enthalpy
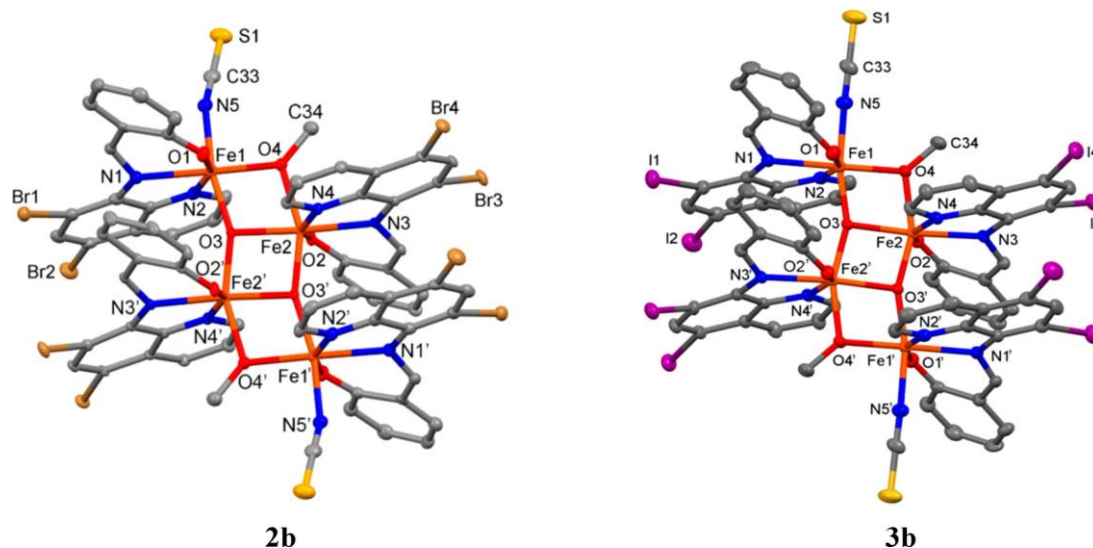
Figure 3. Molecular structure of 2b (left) and 3b (right), with thermal ellipsoids drawn at the 30% probability level. Solvent molecules and hydrogen atoms were removed for clarity. Symmetry code ′ = 1 − x; 1 − y; 1 − z. Color code C = gray, Br = brown, I = violet, O = red, S = yellow, Fe = orange, N = blue, H = white.
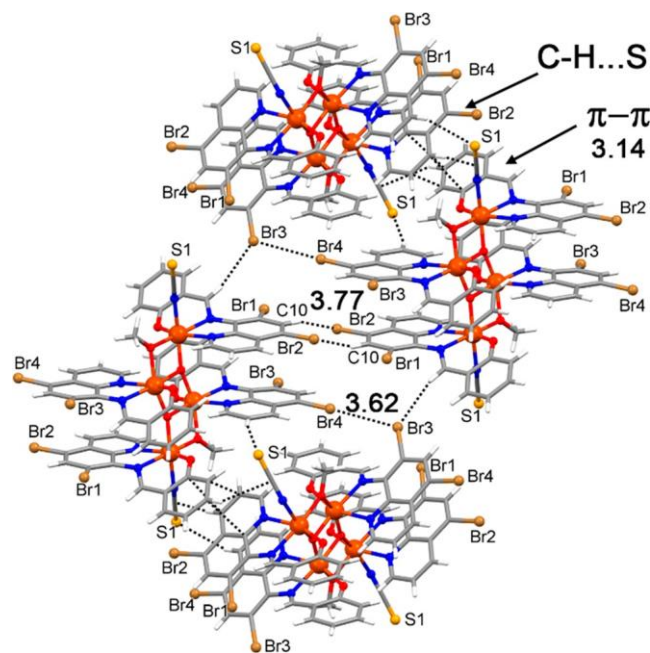

Figure 4. Portion of the crystal packing of 2b. Dashed lines represent short interactions between symmetry related molecules. Selected weak interaction distances are indicated in Å.

contribution ΔH_{SCO} to the spin-crossover (SCO) amounts to 3.84 kcal mol^{-1}, in agreement with the temperature-controlled SCO behavior observed experimentally.[14] The structures of the neutral protonated compounds Hqsal-5,7-X$_2$ (1−3) and the corresponding O-deprotonated (qsal-5,7-X$_2$)$^-$ anions were optimized at the same level of theory. A comparison of the metric parameters calculated for 3 with the corresponding ones determined by single crystal X-ray diffraction (see above) clearly shows an excellent agreement. In particular, it is worth noting that the C−I distances are optimized at values extremely close to the experimental ones (optimized C−I distance = 2.109 Å). Also the formation of the intramolecular O12−H12···N2 bond is reproduced correctly with an optimized O···N distance only

slightly overestimated [calculated 2.598 Å; structural value 2.652(4) Å]. In agreement with the crystal structure analysis, the aminoquinoline moiety is twisted with respect to the plane of the phenyl ring (τ = 44.63°). On passing from 3 to the corresponding deprotonated form qsal-5,7-I$_2$$^-$, the metric parameters remain almost unvaried, with a small decrease in the τ dihedral angle [τ = 39.98° for (qsal-5,7-I$_2$)$^-$] and the loss of planarity of the 2-hydroxyphenylmethanimine moiety. In the deprotonated form, Kohn−Sham (KS) frontier molecular orbitals can be envisaged with large contributions from the lone pairs of electrons located on the two nitrogen and the oxygen atoms (KS-HOMO-6, HOMO-3, and HOMO-1 for (qsal-5,7-I$_2$)$^-$; Figure 7].

These atoms feature remarkable negative natural[61,62] charges Q (Q$_{N1}$ = −0.463, Q$_{N2}$ = −0.504, and Q$_{O12}$ = −0.645 |e|) and are therefore all available to interact with the iron(III) ions. On passing from qsal-5,7-I$_2$$^-$ to the corresponding brominated and chlorinated anions, the natural charges are basically unvaried [(qsal-5,7-Cl$_2$)$^-$: Q$_{N1}$ = −0.465, Q$_{N2}$ = −0.499, and Q$_{O12}$ = −0.650 |e|; (qsal-5,7-Br$_2$)$^-$: Q$_{N1}$ = −0.464, Q$_{N2}$ = −0.500, and Q$_{O12}$ = −0.647 |e|), thus indicating similar donor abilities of the three donor atoms. On varying the nature of the halogen substituents, KS-HOMO-1, KS-HOMO-3, and KS-HOMO-6 keep the same composition in terms of their constituent atomic orbitals, their eigenvalues becoming progressively slightly more stable on passing from (qsal-5,7-I$_2$)$^-$ to (qsal-5,7-Cl$_2$)$^-$ [eigenvalues ε: KS−HOMO-1: −2.082, −2.156, −2.230; HOMO-3: −3.504, −3.570, −3.605; HOMO-6: −4.760, −4.734, and −4.601 eV for (qsal-5,7-Cl$_2$)$^-$, (qsal-5,7-Br$_2$)$^-$, and (qsal-5,7-I$_2$)$^-$, respectively].

DFT calculations have been extended to the monomer cationic complexes [Fe(qsal-5,7-X$_2$)$_2$]$^+$ [X = Cl (1c$^+$), Br (2c$^+$), I (3c$^+$)], identified in solution by mass spectrometry (see above). These complexes, although not isolated in the solid state, represent interesting model complexes of the potential spin crossover (SCO) behavior. In order to model the possible electron configurations, both the HS (S = 5/2, sixtuplet) and LS (S = 1/2, doublet) configurations[63] were modeled for the three Fe^{III} complexes. The optimized structures of complexes 1c$^+$−3c$^+$ show the central ion in a distorted octahedral coordination achieved by the two N1 and N2 atoms and by the O atoms
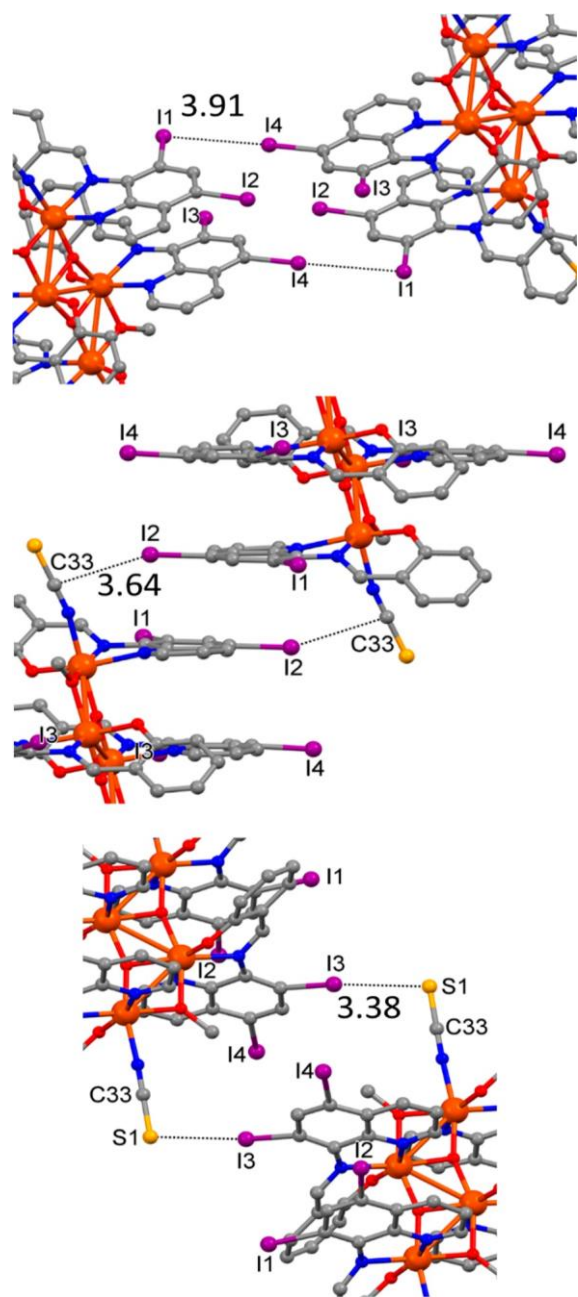
Figure 5. Highlights on the interaction exchanged by the iodine atoms in 3b. Dashed lines represent short interactions between symmetry related molecules, distances are indicated in Å.

(Figure S8 for $1c^+$ in the HS state). Notably, upon coordination the phenyl and the quinolyl rings tend to to a larger degree of coplanarity as compared to the free ligand in order to maximize the interaction to the metal ion (for example, $\tau = 15.73°$ for $1c^+$ in the HS state).

In Table 2, the Fe−N and Fe−O bond lengths optimized for $1c^+$, $2c^+$, and $3c^+$ both in the LS and HS states are listed, showing that the nature of the halogen affects only marginally the bond distances, which depend as expected on the spin state.

An examination of the crystal structures of compounds 1a, 2a, and 3a clearly shows that Fe−O distances fall in the range 1.92−1.94 Å, Fe−N1 bond lengths are all around 2.18 Å, while Fe−N2 distances are slightly shorter (2.13 Å). Therefore, the structural

parameters clearly point to a HS configuration of the complexes.

Accordingly, the total electronic energies calculated for HS and LS complexes $1c^+$−$3c^+$ in the gas phase testify to a larger stability of HS as compared to LS, with energy differences ΔE_{SCO} of 3.0, 3.2, and 3.5 kcal mol^{-1} for $1c^+$, $2c^+$, and $3c^+$, respectively, which are only slightly larger than those calculated for 4 at the same level of theory. A thermochemical analysis shows that by taking into account the zero point energy (ZPE) corrections and the thermal corrections to enthalpy, the same trend is confirmed ($\Delta H_{SCO} = 4.07$, 4.28, and 4.52 kcal mol^{-1} for $1c^+$, $2c^+$, and $3c^+$, respectively). The sum of electronic and thermal free energy calculated for HS and LS model complexes in the gas phase ($\Delta G_{SCO} = 7.59$, 7.91, and 7.90 kcal mol^{-1} for $1c^+$, $2c^+$, and $3c^+$, respectively) shows that the entropy term is essentially independent of the nature of the halogen ($\Delta S_{SCO} = 1.18 \times 10^{-2}$, 1.22×10^{-2}, and 1.13×10^{-2} kcal mol^{-1} for $1c^+$, $2c^+$, and $3c^+$, respectively), so that $T_{1/2}$ depends exclusively on the enthalpy term ($|\Delta H_{LS-HS}/\Delta S_{LS-HS}| = 344$, 351, and 359 for $1c^+$, $2c^+$, and $3c^+$, respectively). The trend in the ΔH_{SCO} values was confirmed when solvation was implicitly considered at the IEF-PCM SCRF level[64] ($\Delta E_{SCO} = 2.49$, 2.78, and 3.11 kcal mol^{-1}; $\Delta H_{SCO} = 3.50$, 3.73, and 4.62 kcal mol^{-1} for $1c^+$, $2c^+$, and $3c^+$, in CHCl$_3$, respectively).

These results strongly testify to an SCO nature of the complexes $1c^+$−$3c^+$, both in the solid state and in chloroform solution. Therefore, theoretical results suggest that while monomers could possibly show a SCO behavior, the formation of complexes with an even number of metal ions results in the strong antiferromagnetic interactions, evidenced experimentally (see above), that prevent any SCO behavior in the solid state. In order to verify this hypothesis, the electronic structure of 1a was investigated at the same level of theory, in the open- and closed-shell singlet configurations ($2S + 1 = 1$, $1a^{sing}$), as an independent HS Fe^{III}−Fe^{III} complex without coupling ($2S + 1 = 11$, $1a^{HS-HS}$), and eventually as an antiferromagnetic singlet ($1a^{afc}$). The latter configuration was obtained by using a broken symmetry approach[65] from a guess of the ground state defined by molecular fragments, including one [Fe(qsal-5,7-X$_2$)]$^{2+}$ ion with five unpaired α-spin electrons (sextet), and another one with five β-spin electrons (sextet). The resulting wave function was optimized to avoid restricted/unrestricted spin instabilities and the geometry of the complex was finally reoptimized. In Table 3 some selected bond lengths are listed for the examined electronic configurations, along with the total electronic energies and spin densities (Figure S10) calculated for $1a^{sing}$, $1a^{HS-HS}$, and $1a^{afc}$.

A comparison of the optimized bond lengths and angles clearly shows that only the configurations of $1a^{HS-HS}$ and $1a^{afc}$ reproduce reliably the coordination pattern at the iron(III) centers. In addition, the closed-shell singlet displays, as expected, a RHF/UHF instability. The total electronic energies calculated for $1a^{HS-HS}$ and $1a^{afc}$ are consistent with the antiferromagnetic state being the ground state, in perfect agreement with the magnetic measurements discussed above. Notably, the spin densities of ±4.29 |e|/au^3 (Figure S10) are in excellent agreement with five unpaired electrons on each Fe^{III} center, since part of the spin density delocalizes onto the ligands.

CONCLUSIONS

A new series of the tridentate N-8-quinolyl-salicylaldimine ligands Hqsal-5,7-X$_2$ (X = Cl(1), Br(2), I(3)) and their corresponding complexes with Fe^{III}, formulated as [Fe(qsal-5,7-X$_2$)(NCS)(MeO)]$_2$·solv. (X = Cl (1a), Br (2a), I (3a)), [Fe^{III}(qsal-5,7-X)$_4$(NCS)$_2$(MeO)$_2$]·solv. (X = Br (2b), I (3b; solv = 4 CH$_2$Cl$_2$), have been synthesized and structurally
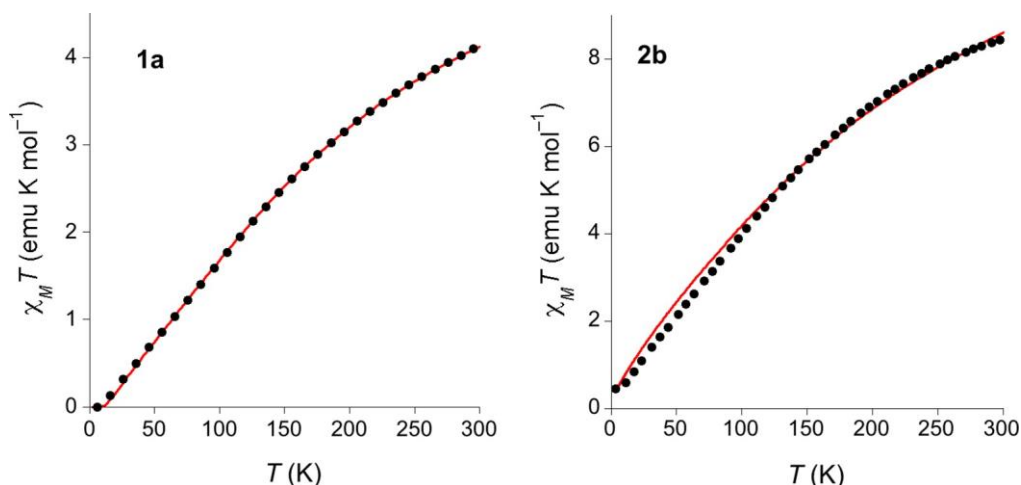
Figure 6. Thermal variation of $\chi_M T$ versus T plots for 1a (left) and 2b (right). In red, the fitting obtained with the following parameters: $g = 2.09$, $J = -21$ K (-14.6 cm^{-1}) (1a) and $g = 2.03$, $J = -35$ K (24.3 cm^{-1}), $J' = -16$ K (11.1 cm^{-1}), (2b).
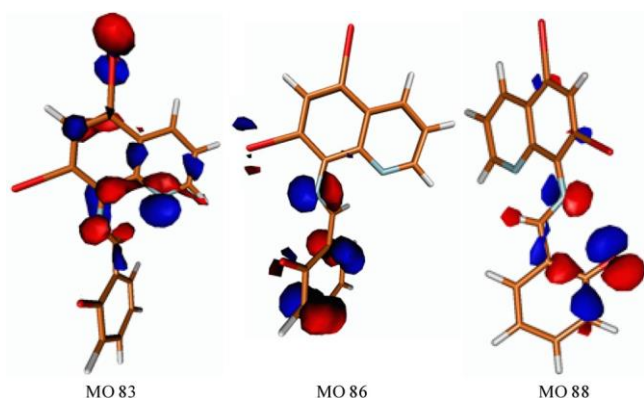

MO 83   MO 86   MO 88

Figure 7. Isosurface drawings of KS-HOMO-6 (MO 83), KS-HOMO-3 (MO 86), and KS-HOMO-1 (MO 88) with large contributions from the LPs on the N and O donor atoms in (qsal-5,7-I$_2$)$^-$. Cutoff value = 0.05 | e|.

Table 2. Fe$-$N and Fe$-$O Bond Distances Optimized for the Model Complexes 1c$^+$$-$3c$^+$ at DFT Level in the Gas Phase in the LS and HS Configurations[a]

		1c$^+$	2c$^+$	3c$^+$
HS	Fe$-$N2	2.131	2.129	2.126
	Fe$-$N1	2.192	2.192	2.192
	Fe$-$O1	1.906	1.908	1.911
LS	Fe$-$N2	1.949	1.947	1.944
	Fe$-$N1	1.994	1.994	1.994
	Fe$-$O1	1.856	1.858	1.860

[a]Labels of the (qsal-5,7-X$_2$)$^-$ ligands as in Figure 2 (X = Cl, Br, and I, for 1c$^+$, 2c$^+$, and 3c$^+$, respectively).

characterized. 1a and 2a are isostructural dimers where each Fe^{III} metal is bound by the N,N,O tridentate qsal-5,7-X$_2$ (X = Cl and Br) ligand, a SCN$^-$ anion, and two bridging methanolate anions in a distorted octahedral environment. The SCN$^-$ anion exhibits a linear geometry since it is bound to the metal center through the nitrogen atom. Several Cl···Cl (3.39 Å) and Br···Br (3.51 Å) halogen intermolecular interactions with symmetry related halogen atoms, CH···S with the aromatic ring and the SCN$^-$ anion, and π−π stacks with adjacent bromoquinoline rings occur between adjacent molecules. In 3a iodine atoms interact through a linear I$_{22}$···S$_1$T geometry with S$_1$T of the SCN$^-$ group via halogen bonding. 2b and 3b are centrosymmetric tetramers where each Fe^{III} is bound by three nitrogen atoms and three oxygen atoms deriving from the tridentate qsal-5,7-X$_2$ (X = Br and I), a SCN$^-$ anion, a bridging methanolate, and a bridging oxy moiety. Unexpectedly, the halo-substitution at the 5,7 position of the aminoquinoline moiety yields dimers and tetramers instead of the mononuclear complexes with a dramatic change of the magnetic properties of the reported complexes, on going from SCO magnetic behavior observed in the mononuclear complexes to strong antiferromagnetic interactions between Fe^{III} centers (S = 5/2), mediated by the alkoxy bridges in dimers and tetramers herein reported.[66,67] DFT calculations support the structural finding, showing that monomers could possibly show an SCO behavior, even though the formation of complexes with an even number of metal ions results in strong antiferromagnetic interactions. DFT clearly shows as well that the antiferromagnetic coupling of the two HS Fe^{III} centers in 1a results in the lowest energy electron configuration of the complex.

In conclusion the search for halogen-bonded systems where halogen-bonds dominate the structure and influence the physical properties of a given material still represents a challenge in material science, even though the results reported in this work show that the proper choice of the halogen substitution on the ligand coordinated to the metal can provide chemists with a versatile strategy for the crystal-engineering design of new compounds with novel physical properties. Further studies will involve the replacement of halogen atoms with different substituents in order to investigate their role, both at the electronic and supramolecular level, in determining the molecular packing pattern and the related physical properties.

◼ EXPERIMENTAL SECTION

Materials. All manipulations were performed in air with reagent grade solvents. All organic chemicals were purchased from TCI (Zentek) and were used without further purification, and inorganic chemicals were purchased from Sigma-Aldrich and used as received. FT-IR spectra were performed on KBr pellets and collected with a Bruker Equinox 55 spectrophotometer. Melting points were obtained on a Kofler hot stage microscope and are uncorrected. Elementary analyses were performed by −CHNS/O PerkinElmer 2400 series II. The aminoquinoline derivative was separated by a chromatographic column (25 mm × 180 mm) filled with DAVISIL silica gel (40−63 m), packed with a Buchi C-670 cartridge.

Table 3. Selected Bond Lengths Calculated for 1a in the Singlet Configuration (1a^{sing}), with Two Independent HS Fe^{III} Ions without Coupling (1a$^{HS\text{-}HS}$), and as an Antiferromagnetic Singlet (1a^{afc})[a]

	1a^{sing}	1a$^{HS\text{-}HS}$	1a^{afc}	Struct.
2S + 1	1	11	1	
Fe−N2	1.946	2.196	2.196	2.139
Fe−N1	1.962	2.206	2.206	2.183
Fe−O1	1.900	1.948	1.948	1.920
Fe−O2/O2′	1.919/1.933	1.981/2.042	1.981/2.042	1.981/2.033
Fe−N1T	1.881	1.972	1.972	2.106
E$_{TOT}$	−7177.6703036	−7177.7815725	−7177.7827629	
spin density on Fe^{III}	0, 0	+4.30, +4.30	+4.29, −4.29[b]	

[a]For each configuration the total electronic energy E$_{TOT}$ (Hartree) and the spin densities (|e|/au^3) on the metal ions are also reported. [b]Figure S10. Labels of the ligand donor atoms as in Figure 2.

Synthesis of 5,7-Dichloro-8-aminoquinoline. A solution of sulfuryl chloride (60.0 mmol) in 12.5 mL of glacial acetic acid was added slowly with stirring to a solution of 8-aminoquinoline (4.38 g, 30.4 mmol) in 21 mL of glacial acetic acid cooled to 10 °C by an ice bath. The mixture was then warmed gradually to room temperature and finally was heated for 25 min on the steam bath at 70−75 °C. Then, the reaction mixture was quenched by a solution of 20 g of sodium acetate in 150 mL of water. The precipitated crude product was removed by filtration and dried in air. Yield: 4.98 g (77%) melting point: 183−184 °C. ESIMS(+): 213.00 m/z (M + H$^+$) with the expected isotope distribution.

Synthesis of 2-[(5,7-Dichloroquinolin-8-ylimino)-methyl]-phenol (Hqsal-5,7-Cl$_2$), 1. 5,7-Dichloro-8-aminoquinoline (3.34 g, 15.7 mmol), salicylaldehyde (2.02 g, 24.3 mmol), and glacial acetic acid (0.34 mL) were dissolved in 40 mL of dry ethanol. The reaction mixture was stirred at room temperature for 14 h. The end of the reaction was verified by TLC (2:8 of diethyl ether/petroleum ether). When the reaction was completed, the mixture reaction was filtered, washed, and dried in air. Yield: 3.74 (74.9%). Melting point: 201 °C. Elem anal. Calcd for C$_{16}$H$_{10}$Cl$_2$N$_2$O (found), mass %: C, 60.59 (59.73); H, 3.18 (2.94); N, 8.33 (8.55). FTIR: νmax(KBr)/cm^{-1} 3435 (νOH), 3057, 2921 (νCH), 1621 (νC●N). ^{1}H NMR (DMSO-d$_6$/DCl): δ = 13.45 (s), 9.41 (s), 9.25 (dd), 8.89 (dd), 8.06 (s), 7.86 (m), 7.78 (dd), 7.74 (td), 7.61 (s), 7.37 (d), 7.28 (td). ESIMS(+): 317.1 m/z (M + H$^+$), with expected isotope distribution.

Synthesis of 5,7-Dibromo-8-aminoquinoline. N-Bromosuccinimide (2.44 g, 13.0 mmol) was added slowly to a stirred solution of 8-aminoquinoline (1.0 g, 6.9 mmol) and 1.4 g, of NaClO$_4$/SiO$_2$ a 1:4 ratio in CH$_2$Cl$_2$ (20 mL). The reaction mixture was stirred at room temperature for 5−10 min, and the progress was controlled by TLC (50:50 of diethyl-ether/petroleum ether). When the reaction was completed, the mixture was filtered, and the catalyst washed with CH$_2$Cl$_2$ (2 × 10 mL). Then, the combined organic layer was washed with water, dried over anhydrous sodium sulfate, and concentrated under reduced pressure using a rotary evaporator. Further purification was carried out by flash chromatography on silica gel (diethyl ether/petroleum ether: 4/6). Yield: 1.39 (66.9%). Melting point: 143 °C. ESIMS(+): 303.1 m/z (M + H$^+$) with expected isotope distribution.

Synthesis of 2-[(5,7-Dibromoquinolin-8-ylimino)-methyl]-phenol (Hqsal-5,7-Br$_2$), 2. 5,7-Dibromo-8-aminoquinoline (1.60 g, 5.3 mmol), salicylaldehyde (1.00 g, 8.1 mmol), and glacial acetic acid (0.1 mL) were dissolved in dry ethanol (40 mL). The reaction mixture was stirred at room temperature for 22 h. The end of the reaction was verified by TLC (diethyl ether/petroleum ether 2:8). When the reaction was completed, the mixture reaction was filtered, washed, and dried in air. Yield: 1.9 g (89.0%). Melting point: 180 °C with decomposition. Elem anal. Calcd for C$_{16}$H$_{10}$Br$_2$N$_2$O (found), mass %: C, 47.33 (46.68); H, 2.48 (2.23); N, 6.90 (6.64). FTIR: νmax(KBr)/cm^{-1} 3435 (νOH), 3049, 2962 (νCH), 1621 (νC●N). ^{1}H NMR (DMSO-d$_6$/DCl): δ = 13.32 (s), 9.30 (s), 9.19 (dd), 8.84 (dd), 8.41 (s), 7.84 (m), 7.76 (dd), 7.72 (td), 7.54 (s), 7.36 (d), 7.27 (td). ESIMS(+): 404.9 m/z (M + H$^+$), with expected isotope distribution.

Synthesis of 5,7-Diiodo-8-aminoquinoline. Potassium iodide (1.0 g, 6.0 mmol) was added slowly to a stirred solution of 8-aminoquinoline (0.43 g, 3.0 mmol), NaIO$_4$ (1.28 g, 6.0 mmol), and NaCl (0.69 g, 12.0

mmol) in 40 mL of acetic acid/water (9/1). The reaction mixture changed from orange to black, and then it was stirred at room temperature for 3 h. When the reaction was completed to the mixture was added 30 mL of water, extracted with CH$_2$Cl$_2$ (3 × 20 mL). Then, the combined organic layer was dried over anhydrous sodium sulfate and concentrated under reduced pressure using a rotary evaporator. Further purification was carried out by flash chromatography on silica gel (diethyl ether/petroleum ether: 1/1). Yield: 0.66 g (44.0%) Melting point: 144−145 °C with decomposition. ESIMS(+): 397.1 m/z (M + H$^+$).

Synthesis of 2-[(5,7-Diiodoquinolin-8-ylimino)-methyl]-phenol (Hqsal-5,7-I$_2$), 3. 5,7-Diiodo-8-aminoquinoline (0.58 g, 1.5 mmol), salicylaldehyde (0.39 g, 1.6 mmol), and glacial acetic acid (0.1 mL) were dissolved in dry ethanol (20 mL). The reaction mixture was stirred at room temperature for 14 h. The end of the reaction was verified by TLC (2/8 of diethyl ether/petroleum ether). When the reaction was completed, the mixture reaction was filtered, washed, and dried in air. Yield: 0.35g (48.0%). Melting point: 173−174 °C with decomposition. Elem anal. Calcd for C$_{16}$H$_{10}$I$_2$N$_2$O (found), mass %: C, 38.43 (39.12); H, 2.02 (2.31); N, 5.60 (5.32). FTIR: νmax(KBr)/cm^{-1} 3441 (νOH), 3057, 2921 (νCH), 1612 (νC●N). ^{1}H NMR (DMSO-d$_6$/DCl): δ = 13.19 (s), 9.23 (s), 9.17 (dd), 8.95 (s), 8.75 (dd), 7.86 (m), 7.81 (m), 7.62 (s), 7.44 (d), 7.34 (td). Mass spectrometry (MS): 501.1 m/z (M + H$^+$).

Synthesis of [Fe(qsal-5,7-Cl$_2$)(NCS)(MeO)]$_2$ (1a). Compound 1 (20.0 mg, 0.06 mmol) was dissolved in CH$_2$Cl$_2$ (5 mL) with Et$_3$N (8.36 μL, 0.06 mmol) to give a yellow solution and was layered at the bottom of test tube. FeCl$_3$·6H$_2$O (8.10 mg, 0.03 mmol) in 1.5 mL of MeOH and NaSCN (2.68 mg, 0.03 mmol) in 1.5 mL of MeOH were sonicated for 5 min to give dark purple solution and were carefully layered on top of the above layer. A blank solution of MeOH (1 mL) was layered in between the above-mentioned solutions. Dark red crystals were formed at the interface after 5 days. Yield = 54.5%. Elem Anal. Calcd for C$_{36}$H$_{24}$Cl$_4$Fe$_2$N$_6$O$_4$S$_2$ (found), mass %: C, 46.88 (47.12); H, 2.62 (2.54); N, 9.11(8.87), Cl 15.38(15.22), O 6.94(6.95), S 6.95(6.56), Fe 12.11(12.01). FTIR: νmax(KBr)/cm^{-1} 2920 (νAr−H), 2061 (νC●N), 1605 (νC●N). MS (ESI+): m/z 688 [Fe(qsal-Cl$_2$)]$^+$.

Synthesis of [Fe(qsal-5,7-Br$_2$)(NCS)(MeO)]$_2$ (2a), [Fe$_4$(qsal-Br$_2$)$_4$-(NCS)$_2$(MeO)$_2$] (2b). The synthetic procedure of 2a was the same as 1a but using 2 (25.0 mg, 0.06 mmol) instead of 1. The use of a very slight excess of Et$_3$N (10.03 μL, 0.07 mmol) yielded 2b. Yield = 56.7% (2a) and 48% (2b). Elem Anal. Calcd C$_{36}$H$_{24}$Br$_4$Fe$_2$N$_6$O$_4$S$_2$ 2a (found), mass %: C, 39.31 (39.12); H, 2.2 (2.31); N, 7.64 (7.32) Br, 29.05(28.62); O 5.82(5.78), S 5.83(5.56), Fe 10.15(10.91) Elem Anal. Calcd C$_{68}$H$_{42}$Br$_8$Fe$_4$N$_{10}$O$_8$S$_2$ 2b (found), mass %: C, 39.77 (39.12); H, 2.06 (1.99); N, 6.82 (6.32) Br, 31.12(30.52); O 6.23 (5.83), S 3.12 (3.42), Fe 10.88 (10.71). FTIR: νmax(KBr)/cm^{-1} 2922 (νAr−H), 2049 (νC●N), 1603 (νC●N). MS (ESI+): m/z 866 [Fe(qsal-Br$_2$)]$^+$.

Synthesis of [Fe(qsal-5,7-I$_2$)(NCS)(MeO)]$_2$ (3a), [Fe$_4$(qsal-5,7-I$_2$)$_4$-(NCS)$_2$(MeO)$_2$] (3b). The synthetic procedure of 3a was the same as 1a but using 3 (30 mg, 0.06 mmol) instead of 1. The use of a very slight excess of Et$_3$N (10.03 μL, 0.07 mmol) yielded 3b. Yield = 49.34% (3a) and 41% (3b). Elem Anal. Calcd C$_{37}$H$_{28}$Fe$_2$I$_4$N$_6$O$_5$S$_2$ 3a (found), mass %: C, 33.66 (33.75); H, 2.14 (2.39); N, 6.37 (6.22) I, 38.45(37.54); O

6.06 (7.1), S 4.86 (4.74), Fe 8.46(8.26) Elem Anal. Calcd $C_{72}H_{50}Cl_8Fe_4I_8N_{10}O_8S_2$ 3b (found), mass %: C, 31.22 (30.24); H, 1.82 (1.85); N, 5.06 (4.77), Cl 10.24 (8.47) I, 36.66(34.54); O 4.62 (4.35), S 2.32 (2.18), Fe 8.07 (7.6). FTIR: vmax(KBr)/cm^{-1} 2919 (vAr−H), 2054 (vC●N, 3a), 2046 (vC●N, 3b), 1601 (vC⊕N). MS (ESI+): m/z 1054 [Fe(qsal-I$_2$)]$^+$.

X-ray Crystallography. Single crystal data were collected with a Bruker APEX DUO diffractometer with a Quazar MX Multilayer Optics diffractometer (Mo Kα radiation; λ = 0.71073 Å) at 100 K (1a, 2a, and 2b) and with a Bruker Smart APEXII at 200 K (3a and 3b). A summary of data collection and structure refinement for 1a−3a, 2b, and 3b are reported in Table 1. The intensity data were integrated from several series of exposures frames (0.3° width) covering the sphere of reciprocal space.[68] Absorption correction were applied using the program SADABS.[69] The structures were solved by the dual space algorithm implemented in the SHELXT code.[70] Fourier analysis and refinement were performed by the full-matrix least-squares methods based on F2 implemented in SHELXL-2014.[71] Graphical material was prepared with the Mercury 3.9[72] program. CCDC 1812729−1812733 contain the supplementary crystallographic data for this paper.

ESI-MS. Mass spectra were recorded on a triple quadruple QqQ Varian 310-MS mass spectrometer using electrospray ionization (ESI) technique. The mass spectra were recorded in positive ion mode in the m/z 50−1000 range. The sample solutions (10 mg/L) were prepared in CH$_3$OH and infused directly into the ESI source using a Varian HPLC pump with a flow rate of 50 μL/min. Needle, shield, and detector were kept at 4500, 600, and 1450 V respectively. Pressure of nebulizing and drying gas was 40 PSI, housing and drying gas temperature was 60 and 250 °C, respectively.

Magnetic Measurements. Magnetic measurements were carried out on polycrystalline powder samples. Each sample was secured inside a tight gel capsule and transferred into the sample compartment of a Quantum Design MPMS-XL-7T SQUID magnetometer (Quantum Design, Inc., San Diego, CA, USA). Magnetic measurements were carried out under an applied field of 1000 Oe in the 2−300 K temperature range. Pascal's constants were used to estimate the diamagnetic corrections for compounds.

DFT Calculations. Theoretical calculations were performed at the DFT[36] level with the Gaussian 09 commercial suite of programs[73] on the neutral compounds 1−3, the corresponding O-deprotonated compounds (qsal-5,7-X$_2$)$^-$ (X = Cl, Br, I), the monomer iron(III) complex cations [Fe(qsal-5,7-X$_2$)$_2$]$^+$ (1c$^+$, 2c$^+$, 3c$^+$ for X = Cl, Br, I), and the complex cation [Fe(qsal-F)$_2$)]$^+$ (4$^+$).[14] The hybrid functional mPW1PW[54] was adopted along with all-electron Schafer, Horn, and Ahlrichs split-valence plus polarization basis sets (BSs) for all atomic species in the Def2SVP Weigend formulation.[55] The molecular geometry optimizations were performed starting from structural data, when available. For all iron(III) complexes, the calculations were carried out both in the high spin (HS, S = 5/2) and the low spin (LS, S = 1/2) configurations. Tight SCF convergence criteria (SCF = tight keyword) and fine numerical integration grids [Integral(FineGrid) keyword] were used. The ZPE and enthalpy corrections at 298.15 K were calculated for 1c$^+$−3c$^+$ and added to the total electronic energy differences ΔE_{SCO} to calculate the enthalpy differences ΔH_{SCO} between HS and LS. Entropy corrections to the energy differences between HS and LS (ΔS_{SCO}) were calculated from the sum of electronic and thermal enthalpies and free energies (ΔG_{SCO}). It was presumed that the temperature difference from 298.15 K to the room temperature was negligible. The calculations were extended to 1a in the closed- and open-shell singlet configurations (1a^{sing}, 2S + 1 = 1), in the configuration featuring two uncoupled Fe^{III} HS ions (1a^{HS-HS}, 2S + 1 = 11) and in the antiferromagnetic complex (1a^{afc}, 2S + 1 = 1, with 5 α- and 5 β-spin electrons on the two metal centers) following a broken symmetry approach. Accordingly, for 1a^{afc} six fragments were defined at the geometry optimized for 1a^{HS-HS}: two [Fe^{III}(qsal-5,7-X$_2$)$_2$]$^{2+}$ fragments (2S + 1 = 6, charge 2+), two CH$_3$O$^-$ anions (2S + 1 = 1, charge −1), and two SCN$^-$ anions (2S+1 = 1, charge −1). Using the "guess = fragment" option, the wave functions of the fragments were combined to form a guess of the wave function of the whole complex. An MO calculation was then completed for the total complex, and the stability of the resulting wave function was verified

(stable = opt). The complex was eventually reoptimized and the stability of the wave function verified again. The nature of the minima for all the optimized structures were verified by harmonic frequency calculations. Atomic charges were calculated in the framework of the natural bonding orbital (NBO)[56,57] analysis at the optimized geometries at the same level of theory. In order to account for the influence of the solvent on the electron configurations of the compounds, calculations were also carried out in the presence of CHCl$_3$, implicitly taken into account by means of the polarizable continuum model (PCM) approach (linear response; nonequilibrium solvation) in its integral equation formalism variant (IEF-PCM), which describes the cavity of the solute within the reaction field (SCRF) through a set of overlapping spheres.[59] The optimized geometries were investigated by means of the program GaussView 5.0.9.[74] In order to investigate KS-MO isosurfaces, the Molden 5.7[75] program was used in a macOS compiled version.[76]

AUTHOR INFORMATION

Corresponding Author

*E-mail: mercuri@unica.it; fax: (+39)0706754486; tel: (+39) 0706754486.

ORCID ⓘ

Jose-Ramon Galan Mascaros: 0000-0001-7983-9762

Narcis Avarvari: 0000-0001-9970-4494

Luciano Marchio: 0000-0002-0025-1104

Maria Laura Mercuri: 0000-0002-4816-427X

Notes

The authors declare no competing financial interest.

■ REFERENCES

(1) Cavallo, G.; Metrangolo, P.; Milani, R.; Pilati, T.; Priimagi, A.; Resnati, G.; Terraneo, G. The Halogen Bond. Chem. Rev. 2016, 116 (4), 2478−2601.

(2) Brammer, L. Halogen Bonding, Chalcogen Bonding, Pnictogen Bonding, Tetrel Bonding: Origins, Current Status and Discussion. Faraday Discuss. 2017, 203, 485−507.

(3) Desiraju, G. R.; Ho, P. S.; Kloo, L.; Legon, A. C.; Marquardt, R.; Metrangolo, P.; Politzer, P.; Resnati, G.; Rissanen, K. Definition of the Halogen Bond (IUPAC Recommendations 2013). Pure Appl. Chem. 2013, 85 (8), 1711−1713.

(4) Politzer, P.; Murray, J. S.; Clark, T. Halogen Bonding and Other Sigma-Hole Interactions:a Perspective. Phys. Chem. Chem. Phys. 2013, 15 (27), 11178−11189.

(5) Imakubo, T.; Sawa, H.; Kato, R. Novel Radical Cation Salts of Organic P-Donors Containing Iodine Atom(s): The First Application of Strong Intermolecular -I • • X- (X = CN, Halogen Atom) Interaction to Molecular Conductors. Synth. Met. 1995, 73, 117−122.

(6) Song, W.; Martsinovich, N.; Heckl, W. M.; Lackinger, M. Thermodynamics of Halogen Bonded Monolayer Self-Assembly at the Liquid-Solid Interface. Chem. Commun. (Cambridge, U. K.) 2014, 50 (88), 13465−13468.

(7) Ayzac, V.; Raynal, M.; Isare, B.; Idé, J.; Brocorens, P.; Lazzaroni, R.; Etienne, T.; Monari, A.; Assfeld, X.; Bouteiller, L. Probing Halogen−halogen Interactions in Solution. Phys. Chem. Chem. Phys. 2017, 19, 32443−32450.

(8) Khavasi, H. R.; Ghanbarpour, A.; Tehrani, A. A. The Role of Intermolecular Interactions Involving Halogens in the Supramolecular Architecture of a Series of Mn(II) Coordination Compounds. RSC Adv. 2016, 6, 2422−2430.

(9) Walch, H.; Gutzler, R.; Sirtl, T.; Eder, G.; Lackinger, M. Material- and Orientation-Dependent Reactivity for Heterogeneously Catalyzed Carbon-Bromine Bond Homolysis. J. Phys. Chem. C 2010, 114 (29), 12604−12609.

(10) Atzori, M.; Artizzu, F.; Sessini, E.; Marchio, L.; Loche, D.; Serpe, A.; Deplano, P.; Concas, G.; Pop, F.; Avarvari, N.; Mercuri, M. L. Halogen-Bonding in a New Family of Tris(haloanilato)metallate(III) Magnetic Molecular Building Blocks. Dalton Trans. 2014, 43 (19), 7006−7019.

(11) Atzori, M.; Marchio, L.; Clerac, R.; Serpe, A.; Deplano, P.; Avarvari, N.; Mercuri, M. L. Hydrogen-Bonded Supramolecular Architectures Based on Tris(Hydranilato)Metallate(III) (M = Fe, Cr) Metallotectons. Cryst. Growth Des. 2014, 14, 5938−5948.

(12) Mercuri, M. L.; Congiu, F.; Concas, G.; Sahadevan, S. A. Recent Advances on Anilato-Based Molecular Materials with Magnetic And/or Conducting Properties. Magnetochemistry 2017; Vol. 3.17

(13) Atzori, M.; Pop, F.; Auban-Senzier, P.; Gomez-Garcia, C. J.; Canadell, E.; Artizzu, F.; Serpe, A.; Deplano, P.; Avarvari, N.; Mercuri, M. L. Structural Diversity and Physical Properties of Paramagnetic Molecular Conductors Based on Bis(ethylenedithio)tetrathiafulvalene (BEDT-TTF) and the Tris(chloranilato)ferrate(III) Complex. Inorg. Chem. 2014, 53 (III), 7028−7039.

(14) Atzori, M.; Pop, F.; Auban-Senzier, P.; Clerac, R.; Canadell, E.; Mercuri, M. L.; Avarvari, N. Complete Series of Chiral Paramagnetic Molecular Conductors Based on Tetramethyl-Bis(ethylenedithio)-Tetrathiafulvalene (TM-BEDT-TTF) and Chloranilate-Bridged Heterobimetallic Honeycomb Layers. Inorg. Chem. 2015, 54 (7), 3643−3653.

(15) Atzori, M.; Benmansour, S.; Mínguez Espallargas, G.; Clemente-Leon, M.; Abhervé, A.; Gomez-Claramunt, P.; Coronado, E.; Artizzu, F.; Sessini, E.; Deplano, P.; Serpe, A.; Mercuri, M. L.; Gomez García, C. J. A Family of Layered Chiral Porous Magnets Exhibiting Tunable Ordering Temperatures. Inorg. Chem. 2013, 52 (17), 10031−10040.

(16) Phonsri, W.; Macedo, D. S.; Moubaraki, B.; Cashion, J. D.; Murray, K. S. Heteroleptic Iron(III) Spin Crossover Complexes; Ligand Substitution Effects. Magnetochemistry 2016, 2 (1), 3.

(17) Phonsri, W.; Harding, D. J.; Harding, P.; Murray, K. S.; Moubaraki, B.; Gass, I. A.; Cashion, J. D.; Jameson, G. N. L.; Adams, H. Stepped Spin Crossover in Fe(III) Halogen Substituted Quinolylsalicylaldimine Complexes. Dalt. Trans. 2014, 43 (46), 17509−17518.

(18) Phonsri, W.; Macedo, D. S.; Davies, C. G.; Jameson, G. N. L.; Moubaraki, B.; Murray, K. S. Heteroleptic Iron(III) Schiff Base Spin Crossover Complexes: Halogen Substitution, Solvent Loss and Crystallite Size Effects. Dalt. Trans. 2017, 46 (21), 7020−7029.

(19) Harding, D. J.; Sertphon, D.; Harding, P.; Murray, K. S.; Moubaraki, B.; Cashion, J. D.; Adams, H. FeIII Quinolylsalicylaldimine Complexes: A Rare Mixed-Spin-State Complex and Abrupt Spin Crossover. Chem. - Eur. J. 2013, 19 (3), 1082−1090.

(20) Sertphon, D.; Harding, D. J.; Harding, P.; Murray, K. S.; Moubaraki, B.; Cashion, J. D.; Adams, H. Anionic Tuning of Spin Crossover in FeIII- Quinolylsalicylaldiminate Complexes. Eur. J. Inorg. Chem. 2013, 2013 (5−6), 788−795.

(21) Dias, J. C.; Vieira, B.; Santos, I. C.; Pereira, L. C. J.; Gama, V. da. Synthesis and Characterization of Fe(III)(3-CH₃O-qsal)₂PF₆·nH₂O (N = 0, 2). Inorg. Chim. Acta 2009, 362 (6), 2076−2079.

(22) Oshio, H.; Kitazaki, K.; Mishiro, J.; Kato, N.; Maeda, Y.; Takashima, Y. New Spin-Crossover Iron(III) Complexes with Large Hysteresis Effects and Time Dependence of Their Magnetism. J. Chem. Soc., Dalton Trans. 1987, 0, 1341−1347.

(23) Ivanova, T. A.; Ovchinnikov, I. V.; Garipov, R. R.; Ivanova, G. I. Spin Crossover [Fe(qsal)₂]X (X = Cl, SCN, CF₃SO₃) Complexes: EPR and DFT Study. Appl. Magn. Reson. 2011, 40 (1), 1−10.

(24) Hayami, S.; Hiki, K.; Kawahara, T.; Maeda, Y.; Urakami, D.; Inoue, K.; Ohama, M.; Kawata, S.; Sato, O. Photo-Induced Spin Transition of iron(III) Compounds with π-π Intermolecular Interactions. Chem. - Eur. J. 2009, 15 (14), 3497−3508.

(25) Hayami, S.; Gu, Z. Z.; Yoshiki, H.; Fujishima, A.; Sato, O. Iron(III) Spin-Crossover Compounds with a Wide Apparent Thermal Hysteresis around Room Temperature. J. Am. Chem. Soc. 2001, 123 (47), 11644−11650.

(26) Djukic, B.; Poddutoori, P. K.; Dube, P. A.; Seda, T.; Jenkins, H. A.; Lemaire, M. T. Bimetallic iron(3+) Spin-Crossover Complexes Containing a 2,2′-Bithienyl Bridging Bis-QsalH Ligand. Inorg. Chem. 2009, 48 (13), 6109−6116.

(27) Jeon, I.-R.; Jeannin, O.; Clerac, R.; Rouzieres, M.; Fourmigue, M. Spin-State Modulation of Molecular Fe^III Complexes via Inclusion in Halogen-Bonded Supramolecular Networks. Chem. Commun. 2017, 53 (36), 4989−4992.

(28) Djukic, B.; Jenkins, H. A.; Seda, T.; Lemaire, M. T. Structural and Magnetic Properties of Homoleptic iron(III) Complexes Containing N-(8-Quinolyl)-Salicylaldimine [Fe(Qsal)₂]⁺X⁻ {X = I or (Qsal)FeCl₃}. Transition Met. Chem. 2013, 38 (2), 207−212.

(29) Phonsri, W.; Harding, P.; Liu, L.; Telfer, S. G.; Murray, K. S.; Moubaraki, B.; Ross, T. M.; Jameson, G. N. L.; Harding, D. J. Solvent Modified Spin Crossover in an Iron(III) Complex: Phase Changes and an Exceptionally Wide Hysteresis. Chem. Sci. 2017, 8 (5), 3949−3959.

(30) Harding, D. J.; Phonsri, W.; Harding, P.; Gass, I. A.; Murray, K. S.; Moubaraki, B.; Cashion, J. D.; Liu, L.; Telfer, S. G. Abrupt Spin Crossover in an Iron(III) Quinolylsalicylaldimine Complex: Structural Insights and Solvent Effects. Chem. Commun. 2013, 49 (56), 6340.

(31) Harding, D. J.; Phonsri, W.; Harding, P.; Murray, K. S.; Moubaraki, B.; Jameson, G. N. L. Abrupt Two-Step and Symmetry Breaking Spin Crossover in an Iron(III) Complex: An Exceptionally Wide [LS-HS] Plateau. Dalton Trans. 2015, 44 (34), 15079−15082.

(32) Phonsri, W.; Davies, C. G.; Jameson, G. N. L.; Moubaraki, B.; Ward, J. S.; Kruger, P. E.; Chastanet, G.; Murray, K. S. Symmetry Breaking above Room Temperature in an Fe(II) Spin Crossover Complex with an N₄O₂ Donor Set. Chem. Commun. 2017, 53 (8), 1374−1377.

(33) Phonsri, W.; Macedo, D. S.; Vignesh, K. R.; Rajaraman, G.; Davies, C. G.; Jameson, G. N. L.; Moubaraki, B.; Ward, J. S.; Kruger, P. E.; Chastanet, G.; Murray, K. S. Halogen Substitution Effects on N₂O Schiff Base Ligands in Unprecedented Abrupt Fe^II Spin Crossover Complexes. Chem. - Eur. J. 2017, 23 (29), 7052−7065.

(34) Emmanuvel, L.; Shukla, R. K.; Sudalai, A.; Gurunath, S.; Sivaram, S. NaIO₄/KI/NaCl: A New Reagent System for Iodination of Activated Aromatics through in Situ Generation of Iodine Monochloride. Tetrahedron Lett. 2006, 47 (28), 4793−4796.

(35) Zhang, Y.; Shibatomi, K.; Yamamoto, H. Lewis Acid Catalyzed Highly Selective Halogenation of Aromatic Compounds. Synlett 2005, 18, 2837−2842.

(36) Cadoni, E.; Ferino, G.; Pitzanti, P.; Secci, F.; Fattuoni, C.; Nicolò, F.; Bruno, G. Halogen and Hydrogen Bonding Benzothiophene Diol Derivatives: A Study Using Ab Initio Calculations and X-Ray Crystal Structure Measurements. ChemistryOpen 2015, 4 (2), 161−168.

(37) Bagheri, M.; Azizi, N.; Saidi, M. R. An Intriguing Effect of Lithium Perchlorate Dispersed on Silica Gel in the Bromination of Aromatic Compounds by N -Bromosuccinimide. Can. J. Chem. 2005, 83 (2), 146−149.

(38) Bertani, R.; Sgarbossa, P.; Venzo, A.; Lelj, F.; Amati, M.; Resnati, G.; Pilati, T.; Metrangolo, P.; Terraneo, G. Halogen Bonding in Metal-Organic-Supramolecular Networks. Coord. Chem. Rev. 2010, 254 (5−6), 677−695.

(39) Borovina, M.; Kodrin, I.; Đaković, M. Testing the Limits of Halogen Bonding in Coordination Chemistry. CrystEngComm 2018, 20 (5), 539−549.

(40) Politzer, P.; Lane, P.; Concha, M. C.; Ma, Y.; Murray, J. S. An Overview of Halogen Bonding. J. Mol. Model. 2007, 13 (2), 305−311.

(41) Koch, W.; Holthausen, M. C. A Chemist's Guide to Density Functional Theory, 2nd ed., Wiley, 2001; Vol. 3.

(42) Conradie, J.; Ghosh, A. DFT Calculations on the Spin-Crossover Complex Fe(salen)(NO): A Quest for the Best Functional. J. Phys. Chem. B 2007, 111 (44), 12621−12624.

(43) Perdew, J. P.; Chevary, J. A.; Vosko, S. H.; Jackson, K. A.; Pederson, M. R.; Singh, D. J.; Fiolhais, C. Atoms, Molecules, Solids, and Surfaces: Applications of the Generalized Gradient Approximation for Exchange and Correlation. Phys. Rev. B: Condens. Matter Mater. Phys. 1992, 46 (11), 6671−6687.

(44) Perdew, J. P.; Burke, K.; Wang, Y. Generalized Gradient Approximation for the Exchange-Correlation Hole of a Many-Electron System. Phys. Rev. B: Condens. Matter Mater. Phys. 1996, 54 (23), 16533−16539.

(45) Becke, A. D. Density-Functional Exchange-Energy Approximation with Correct Asymptotic Behavior. Phys. Rev. A: At., Mol., Opt. Phys. 1988, 38 (6), 3098−3100.

(46) Becke, A. D. Density-Functional Thermochemistry. III. The Role of Exact Exchange. J. Chem. Phys. 1993, 98 (7), 5648−5652.

(47) Lee, C.; Yang, W.; Parr, R. G. Development of the Colle-Salvetti Correlation-Energy Formula into a Functional of the Electron Density. Phys. Rev. B: Condens. Matter Mater. Phys. 1988, 37 (2), 785−789.

(48) Stephens, P. J.; Devlin, F. J.; Chabalowski, C. F.; Frisch, M. J. Ab Initio Calculation of Vibrational Absorption and Circular Dichroism Spectra Using Density Functional Force Fields. J. Phys. Chem. 1994, 98 (45), 11623−11627.

(49) Salomon, O.; Reiher, M.; Hess, B. A. Assertion and Validation of the Performance of the B3LYP* Functional for the First Transition Metal Row and the G2 Test Set. J. Chem. Phys. 2002, 117 (10), 4729−4737.

(50) Reiher, M.; Salomon, O.; Hess, B. A. Reparameterization of Hybrid Functionals Based on Energy Differences of States of Different Multiplicity. Theor. Chem. Acc. 2001, 107 (1), 48−55.

(51) Kepp, K. P. Theoretical Study of Spin Crossover in 30 Iron Complexes. Inorg. Chem. 2016, 55 (6), 2717−2727.

(52) Sirirak, J.; Sertphon, D.; Phonsri, W.; Harding, P.; Harding, D. J. Comparison of Density Functionals for the Study of the High Spin Low Spin Gap in Fe(III) Spin Crossover Complexes. Int. J. Quantum Chem. 2017, 117 (9), e25362.

(53) Secci, F.; Frongia, A.; Rubanu, M. G.; Sechi, M. L.; Sarais, G.; Arca, M.; Piras, P. P. From (Phenylsulfanyl)cycloalkanecarbaldehydes to Optically Active Spirocyclic Tetrahydrofurans: Stereospecific Resolution of Symmetric Aldehydes through (S)-Proline-Catalysed Aldol Reaction. Eur. J. Org. Chem. 2014, 2014 (30), 6659−6675.

(54) Sancineto, L.; Vargas, J. P.; Monti, B.; Arca, M.; Lippolis, V.; Perin, G.; Lenardao, E. J.; Santi, C. Atom Efficient Preparation of Zinc Selenates for the Synthesis of Selenol Esters under "On Water" Conditions. Molecules 2017, 22 (6).953

(55) Martis, A.; Luridiana, A.; Frongia, A.; Arca, M.; Sarais, G.; Aitken, D. J.; Guillot, R.; Secci, F. Acid-Catalyzed Reaction of 2-Hydroxycyclobutanone with Benzylic Alcohols. Org. Biomol. Chem. 2017, 15 (47), 10053−10063.

(56) Deiana, C.; Aragoni, M. C.; Isaia, F.; Lippolis, V.; Pintus, A.; Slawin, A. M. Z.; Woollins, D. J.; Arca, M. Structural Tailoring of the NIR-Absorption of bis(1,2-Dichalcogenolene) Ni/Pt Electrochromophores Deriving from 1,3-Dimethyl-2-Chalcogenoxo-Imidazoline-4,5-Dichalcogenolates. New J. Chem. 2016, 40 (10), 8206−8210.

(57) Isaia, F.; Aragoni, M. C.; Arca, M.; Caltagirone, C.; Castellano, C.; De Filippo, G.; Garau, A.; Lippolis, V.; Pivetta, T. Gold and Palladium Oxidation/complexation in Water by a Thioamide−iodine Leaching System. Green Chem. 2017, 19, 4591−4599.

(58) Aragoni, M. C.; Arca, M.; Cabras, V.; Coles, S. J.; Ennas, G.; Isaia, F.; Lai, R.; Lippolis, V.; Podda, E. Coordination Polymers Based on Dithiophosphato/dithiophosphonato Nickel Complexes and Linear 1,4-di(3-Pyridyl)buta-1,3-diyne Ligand. Supramol. Chem. 2017, 29 (11), 853−864.

(59) Adamo, C.; Barone, V. Exchange Functionals with Improved Long-Range Behavior and Adiabatic Connection Methods without Adjustable Parameters: The mPW and mPW1PW Models. J. Chem. Phys. 1998, 108 (2), 664−675.

(60) Weigend, F.; Ahlrichs, R. Balanced Basis Sets of Split Valence, Triple Zeta Valence and Quadruple Zeta Valence Quality for H to Rn: Design and Assessment of Accuracy. Phys. Chem. Chem. Phys. 2005, 7 (18), 3297.

(61) Reed, A. E.; Weinstock, R. B.; Weinhold, F. Natural Population Analysis. J. Chem. Phys. 1985, 83 (2), 735−746.

(62) Weinhold, F. Natural Bond Orbital Analysis: A Critical Overview of Relationships to Alternative Bonding Perspectives. J. Comput. Chem. 2012, 33 (30), 2363−2379.

(63) Sertphon, D.; Harding, D. J.; Harding, P.; Murray, K. S.; Moubaraki, B.; Adams, H.; Alkas, A.; Telfer, S. G. Substituent-Influenced Spin Crossover in FeIII Quinolylsalicylaldiminates. Eur. J. Inorg. Chem. 2016, 2016 (3), 432−438.

(64) Tomasi, J.; Mennucci, B.; Cammi, R. Quantum Mechanical Continuum Solvation Models. Chem. Rev. 2005, 105 (8), 2999−3093.

(65) Butschke, B.; Fillman, K. L.; Bendikov, T.; Shimon, L. J. W.; Diskin-Posner, Y.; Leitus, G.; Gorelsky, S. I.; Neidig, M. L.; Milstein, D. How Innocent Are Potentially Redox Non-Innocent Ligands? Electronic Structure and Metal Oxidation States in Iron-PNN Complexes as a Representative Case Study. Inorg. Chem. 2015, 54 (10), 4909−4926.

(66) Fourmigue, M. Halogen Bonding in Conducting or Magnetic Molecular Materials. In Halogen Bonding: Fundamentals and Applications; Mingos, D. M. P., Eds.; Springer: Berlin, 2008; pp 181−207.

(67) Fourmigue, M.; Batail, P. Activation of Hydrogen- and Halogen-Bonding Interactions in Tetrathiafulvalene-Based Crystalline Molecular Conductors. Chem. Rev. 2004, 104 (11), 5379−5418.

(68) SMART (Control) and SAINT (Integration) Software for CCD Systems; Bruker AXS: Madison, WI, 1994.

(69) Madison, W. I. Area-Detector Absorption Correction; Siemens Industrial Automation Inc., 1996.

(70) Sheldrick, G. M. SHELXT - Integrated Space-Group and Crystal-Structure Determination. Acta Crystallogr., Sect. A: Found. Adv. 2015, 71 (1), 3−8.

(71) Sheldrick, G. M. Crystal Structure Refinement with SHELXL. Acta Crystallogr., Sect. C: Struct. Chem. 2015, 71 (Md), 3−8.

(72) Macrae, C. F.; Edgington, P. R.; McCabe, P.; Pidcock, E.; Shields, G. P.; Taylor, R.; Towler, M.; van de Streek, J. Mercury: Visualization and Analysis of Crystal Structures. J. Appl. Crystallogr. 2006, 39, 453−457.

(73) Frisch, M. J.; Trucks, G. W.; Schlegel, H. B.; Scuseria, G. E.; Robb, M. A.; Cheeseman, J. R.; Scalmani, G.; Barone, V.; Mennucci, B.; Petersson, G. A.; Nakatsuji, H.; Caricato, M.; Li, X.; Hratchian, H. P.; Izmaylov, A. F.; Bloino, J.; Zheng, G.; Sonnenberg, J. L.; Hada, M.; Ehara, M.; Toyota, K.; Fukuda, R.; Hasegawa, J.; Ishida, M.; Nakajima, T.; Honda, Y.; Kitao, O.; Nakai, H.; Vreven, T.; Montgomery, J. A., Jr.; Peralta, J. E.; Ogliaro, F.; Bearpark, M.; Heyd, J. J.; Brothers, E.; Kudin,

K. N.; Staroverov, V. N.; Kobayashi, R.; Normand, J.; Raghavachari, K.; Rendell, A.; Burant, J. C.; Iyengar, S. S.; Tomasi, J.; Cossi, M.; Rega, N.; Millam, J. M.; Klene, M.; Knox, J. E.; Cross, J. B.; Bakken, V.; Adamo, C.; Jaramillo, J.; Gomperts, R.; Stratmann, R. E.; Yazyev, O.; Austin, A. J.; Cammi, R.; Pomelli, C.; Ochterski, J. W.; Martin, R. L.; Morokuma, K.; Zakrzewski, V. G.; Voth, G. A.; Salvador, P.; Dannenberg, J. J.; Dapprich, S.; Daniels, A. D.; Farkas, O.; Foresman, J. B.; Ortiz, J. V.; Cioslowski, J.; Fox, D. J. Gaussian 09, revision D.01; Gaussian, Inc.: Wallingford, CT, 2009.

(74) Dennington, R.; Keith, T.; Millam, J. GaussView, Version 5.0.8; Semichem Inc., 2009, S. M. K. Tetrahydroxyquinone.

(75) Schaftenaar, G.; Noordik, J. H. Molden: A Pre-and Post-Processing Program for Molecular and Electronic Structures. J. Comput.-Aided Mol. Des. 2000, 14, 123−134.

(76) See http://people.unica.it/massimilianoarca/lang/it/2018/02/13/compiling-molden-5-7-on-macos-high-sierra-how-to.